Sustainable Energy & Fuels

ROYAL SOCIETY OF CHEMISTRY

PAPER

View Article Online
View Journal | View Issue

Check for updates

Cite this: *Sustainable Energy Fuels*, 2025, **9**, 5044

Received 14th April 2025
Accepted 29th June 2025

DOI: 10.1039/d5se00527b

rsc.li/sustainable-energy

Experimental and computational analysis of Ni–P and Fe–P metal foams for enhanced hydrogen evolution reaction in alkaline media†

Natália Podrojková,[a] Alexandra Gubóová,[b] Magdalena Streckova,[b] František Kromka[b] and Renáta Oriňaková *[ac]

Electrochemical water splitting is a promising approach for sustainable hydrogen production, with the hydrogen evolution reaction (HER) playing a key role. Transition metal phosphides (TMPs) have emerged as efficient and cost-effective alternatives to Pt-based catalysts. In this study, we investigate Ni–P and Fe–P metal foams, utilising their porous structures to enhance catalytic activity. Electrochemical analysis reveals that Ni–P exhibits superior reaction kinetics (79 mV dec^{-1}) and a high electrochemically active surface area (41.8 mF cm^{-2}). Density functional theory (DFT) calculations further confirm the role of phosphorus doping, with Ni(111)P_{ads} achieving a near-optimal Gibbs free energy ($\Delta G_{H^*} = 0.01$ eV). Comparative DFT analysis also reveals a trend in ΔG_H values for Ni(111) and Fe(110), demonstrating the impact of phosphorus incorporation on HER performance. These findings provide valuable insights into the design of porous TMP catalysts for efficient and scalable hydrogen production.

Introduction

Due to its environmental amiability and clean and sustainable properties, hydrogen (H_2) is a potential energy source that will fulfil future energy demands.[1,2] One of the most effective methods for producing green H_2 as a clean fuel with substantial energy density, generated from renewable energy sources, is electrochemical water splitting.[3–6]

Electrochemical water splitting involves two half-reactions: the hydrogen evolution reaction (HER) occurs at the cathode, and the oxygen evolution reaction (OER) takes place at the anode.[6,7] Using an alkaline electrolyte, HER is undertaken in two steps, as shown in the equations below (eqn (1) and (2)).[8–10]

$$H_2O + e^- \rightarrow H^* + OH^- \text{ (Volmer)} \quad (1)$$

$$H_2O + e^- + H^* \rightarrow H_2 + OH^- \text{ (Heyrovsky)} \quad (2)$$

or

$$2H^* \rightarrow H_2 \text{ (Tafel)} \quad (3)$$

The formation of adsorbed hydrogen H* results from reducing water molecules by transferring an electron ($H_2O + e^- \rightarrow H^* + OH^-$). Subsequently, gaseous H_2 is formed through either the Heyrovsky or Tafel reaction steps, based on the H* coverage ratio.[11,12]

The current yield of global hydrogen supply from electrochemical water splitting accounts for only 4%.[6] One reason is the use of precious metals, such as platinum (Pt). Pt-based catalysts exhibit remarkably low overpotentials, making them the most efficient electrocatalysts for HER.[13] However, their use significantly increases the overall cost of the process due to the limited availability and high costs associated with precious metal materials.[14] Besides, the kinetics of Pt-catalysed HER significantly decline by two to three orders of magnitude when using an alkaline electrolyte instead of acid.[14,15] Therefore, there is a pressing need to develop cost-effective and abundantly available catalysts to facilitate HER in alkaline media.

Metal phosphide electrocatalysts have garnered considerable attention due to the advantageous interactions between phosphorus and metal atoms, resulting in a similar effect to that of Pt-based catalysts.[10,16] These interactions result in enhanced conductivity, superior resistance to corrosion, and notable catalytic performance.[10] Despite their potential, the effectiveness of metal phosphides is still lower than that of Pt-based catalysts, emphasising a need to enhance their electrocatalytic performance. It is widely recognised that composition, structure, morphology, and surface/interface characteristics significantly influence their electrocatalytic performance.[5]

Among the various investigated traditional iron or nickel phosphide nanoparticles, Ni–P and Fe–P metal foams have

---

[a] *Institute of Chemistry, Faculty of Science, P. J. Safarik University, Moyzesova 11, 040 01 Kosice, Slovak Republic. E-mail: renata.orinakova@upjs.sk*

[b] *Institute of Materials Research, Slovak Academy of Sciences, Watsonova 47, 040 01 Kosice, Slovak Republic*

[c] *Centre of Polymer Systems, Tomas Bata University in Zlín, Třída Tomáše Bati 5678, 760 01 Zlín, Czech Republic*

† Electronic supplementary information (ESI) available. See DOI: **https://doi.org/10.1039/d5se00527b**

emerged as particularly promising due to their several key advantages as electrocatalysts. First, their three-dimensional, porous architecture provides a large surface area, enabling efficient gas bubble release during electrolysis and reducing mass transport limitations. Second, as bulk, self-supporting electrodes, these foams eliminate the need for binders or conductive additives typically required to process nanoparticle catalysts into functional electrodes, thus minimising interfacial resistance and enhancing overall electrical conductivity. Third, the mechanical robustness of the foam structure offers superior durability and stability under prolonged electrochemical operation, addressing a common challenge faced by nanoparticle-based catalysts, which often suffer from detachment or degradation over time. These combined features make metal phosphide foams auspicious materials for scalable and practical electrocatalytic applications. Additionally, recent advancements in hierarchical and ultrathin bifunctional foam electrocatalysts, such as NiCoP@FeNi LDH supported on Ni foam[17] and FeCoV-doped NiMOF nanosheet arrays,[18] demonstrate exceptional HER and OER activity even at industrial-scale current densities. Foam materials reinforce the potential of 3D-structured, non-noble electrocatalysts for practical hydrogen production applications. Therefore, we review the current literature on Ni–P, Fe–P, and NiFe–P foams below and present a benchmark table (Table 1).

Ni–P foam electrocatalysts

Nickel–phosphorus (Ni–P) alloys and phosphides on nickel foam have recently demonstrated excellent alkaline HER activity. Amorphous Ni–P films electrodeposited on Ni foam can achieve very low overpotentials and Tafel slopes across a wide pH range. Silva *et al.* prepared an optimal 3-Ni–P film on Ni foam (3-Ni–P/NF) *via* one-step electrodeposition, which required an overpotential of 69 mV to achieve 10 mA cm^{-2} in 1 M KOH.[19] 3-Ni-P/NF exhibited a Tafel slope of ~71 mV dec^{-1} in alkaline solution, indicating favourable Volmer–Heyrovsky kinetics. Its double-layer capacitance (C_{dl}) was ~10 mF cm^{-2}. Notably, the 3-Ni-P/NF electrode was stable, as demonstrated by durability tests at −100 mA cm^{-2} for 16 hours, during which it showed negligible degradation. In contrast, electroless Ni–P films doped with ultralow Pt have achieved near-Pt-like HER activity. Battiato *et al.* reported that a Ni–P film on Ni foam immersed in Pt NPs solution 5 times (5-Pt/Ni–P/NF) needed just 22 mV for achieving 10 mA cm^{-2} in 1 M KOH.[20] This catalyst exhibited a Tafel slope of approximately 30–40 mV dec^{-1} in the low overpotential range, indicating rapid Volmer steps.

Fe–P foam electrocatalysts

Recent advancements in iron phosphide (Fe–P) electrocatalysts supported on mainly Ni foam substrates have demonstrated promising activity and stability for the hydrogen evolution reaction (HER) in alkaline media, particularly in 1.0 M KOH. Notably, Zhang *et al.* synthesised Ru-doped FeP nanosheets directly grown on Fe foam (Ru–FeP@FF), which exhibited an ultralow overpotential of 31 mV at 10 mA cm^{-2} and a low Tafel slope of 42.6 mV dec^{-1}, underscoring its excellent catalytic kinetics.[21] However, stability was moderate at 24 h. Alothman *et al.* prepared a comparable high-performing catalyst, FeP/Co_3O_4/CF, integrated onto Co foam *via* a pre-oxidation route.[22] FeP/Co_3O_4/CF delivered a slightly higher overpotential of 52 mV, along with a superior Tafel slope of 29 mV dec^{-1} and exceptional long-term stability of up to 150 h, indicating its potential for industrial applications. In contrast, Zhong *et al.* encapsulated FeP in an N, P co-doped carbon matrix on Ni foam (FeP@NPC/NF-450), which showed a higher overpotential of 106.1 mV and a Tafel slope of 110.7 mV dec^{-1}.[23] This reflected a trade-off between protection from corrosion and kinetic efficiency. Qi *et al.* developed phosphorus-deficient CoP–FeP heterostructure on Ni foam (Vp–CoP–FeP/NF), which achieved 58 mV overpotential and a 70.6 mV dec^{-1} Tafel slope.[24] The catalyst performed over 50 h, benefiting from the synergistic interplay of P vacancies and interfacial effects. Collectively, these findings reveal that rational interface engineering, heteroatom doping, and substrate integration are crucial strategies for optimising the HER performance of Fe–P-based foam electrocatalysts. Notably, the incorporation of metal and the formation of composites offer particularly promising pathways toward scalable alkaline hydrogen production.

NiFe–P foam electrocatalysts

Bimetallic Ni–Fe–P electrocatalysts often outperform their monometallic counterparts due to synergistic effects between

Table 1 Comparative performance benchmarks of recent Ni–P, Fe–P, and NiFe–P-based electrocatalysts for the HER in 1 M KOH. Key metrics include overpotential at 10 mA cm^{-2} (η_{10}), Tafel slope (b), double-layer capacitance (C_{dl}), and stability duration[a]

Catalyst	Electrolyte	η_{10} [mV]	b [mV.dec^{-1}]	C_{dl} [mF cm^{-2}]	Stability/durability [h]	References
3-Ni-P/NF	1 M KOH	69	71	10.03	16	19
5-Pt/Ni–P/NF	1 M KOH	22	30	7.9	15	20
Ru–FeP@FF	1 M KOH	31	42.6	169.7	24	21
FeP/Co_3O_4/CF	1 M KOH	52	29	42.4	150 (100 mV)	22
FeP@NPC/NF-450	1 M KOH	106.1	110.7	6.7	48	23
V_p–CoP–FeP/NF	1 M KOH	58	70.6	101.3	50	24
NiFeP/NiF	1 M KOH	102	101	20.4	1100 (300 mV)	25
NiFeP/NiF	1 M KOH	93	79.2	0.019	15	26

[a] NF – Ni foam; FF – Fe foam.

Ni and Fe. A prominent example is the work by Dong *et al.*,[25] who prepared NiFeP composite nanosheets on Ni foam *via* a mild wet-chemical synthesis process followed by *in situ* phosphorisation. The NiFeP/Ni foam catalyst achieved an HER overpotential of 102 mV at 10 mA cm^{-2} in 1 M KOH with a Tafel slope of 101 mV dec^{-1}. The temperature-controlled synthesis of NiFeP enables the tuning of its morphology and activity. Li and Wu prepared NiFeP on Ni foam at various hydrothermal temperatures (100–160 °C), followed by phosphorisation.[26] The NiFeP/NiF sample prepared at 140 °C exhibited the best performance, with a current density of 93 mV at 10 mA cm^{-2} and a Tafel slope of 79.2 mV dec^{-1} in KOH. The NiFeP-140 also exhibited the largest ECSA with C_{dl} of 0.019 mF cm^{-2}, confirming that its 3D interconnected microsphere structure exposes a larger active area. Recently, Gubóová *et al.* focused on the synthesis and electrochemical study of NiP, FeP, and NiFeP metal foams in alkaline media,[27] as porous electrodes are commonly employed to reduce the overpotential associated with HER, which is achieved by increasing the surface area.[28] NiP catalysts exhibited exceptional electroactivity, demonstrated by a low Tafel slope of 37.3 mV dec^{-1}.

Computational studies of Ni-, Fe- and NiFeP electrocatalysts

To better understand the behaviour of given metal foams, further research is necessary, which can be supported by employing density functional theory (DFT) calculations. When examining the computational literature focused on NiP or FeP-based catalysts, it becomes evident that only a limited number of computational studies have been conducted for NiP. In contrast, several studies, including those on FeP foams, have been performed for FeP in combination with other metals or phosphides. Hu *et al.* investigated the introduction of the P atom in the NiP_2 structure, which accordingly altered the adsorption sites of H atoms, leading to a decrease in the adsorption free energy of H atoms and thereby enhancing the HER activity compared to pure Ni catalysts.[29] Recently, Zhao *et al.* prepared and studied NiP/Fe_3P/MoP@NF nanoblocks using DFT calculations.[30] Their research revealed the highest Gibbs free energy (ΔG°_{H*}) of 0.55 eV for NiP(002), which incorporates P atoms in the catalyst surface. Regarding FeP catalysts, several research groups have investigated FeP foams for water splitting using DFT calculations. Zhang *et al.* synthesised V-doped FeP nanoflowers grown on Fe foam for HER and studied FeP and V–FeP surfaces using DFT calculations.[31] According to their findings, the energy barrier for H_2O dissociation is lower for V–FeP (0.38 eV) than for FeP (0.41 eV). Cui *et al.* synthesised Ru–FeP_4 nanosheets grown on Fe foam as bifunctional catalysts for H_2 production and supplemented their research with DFT calculations of FeP_4 and Ru–FeP_4 surfaces.[32] The ΔG_{H*} of Ru–FeP_4 (−0.18 eV) was significantly closer to the ideal ΔG_{H*} value than FeP_4 (−0.31 eV), suggesting that Ru-doping enhances the catalytic activity towards HER.

To enhance comprehension of our findings when applying metal foams in HER, we combined our experimental research with a computational investigation focused on the interactions between Ni and Fe surfaces and the P atom described in this paper. Besides synthesis and electrochemical examination of Ni–P and Fe–P metal foams, Ni(111) and Fe(110) surfaces with adsorbed P atoms are computationally prepared, and adsorption of H* atom is conducted to compare adsorption energies E_{ads} and Gibbs free energies ΔG_{H*}. This approach was chosen to simplify the modelling process and provide a clearer understanding of the fundamental interactions. Most prior studies have focused on complex surface models, often overlooking the effects of individual metal surfaces interacting with phosphorus. Additional experimental results are supplemented to support the computational research.

Results and discussion

Surface and structural characterisation of foam catalysts

X-ray diffraction analysis (XRD) corroborated the phase composition and crystalline structure of the samples. The results are depicted in Fig. 1. The Fe foam exhibited a cubic structure with a space group of $Im\bar{3}m$ (reference code 00-006-0696). The prominent diffraction peaks observed at 2θ values of 52.379°, 77.237°, and 99.708° corresponded to the (110), (200), and (211) planes, respectively. After the phosphorisation process described above, a new minority phase with reflections at 41.4°, 43.5°, 54.4°, 55.3°, 54.4°, and 56.8° corresponding to the (102), (111), (112), (202), and (56.8) planes were identified as FeP in the orthorhombic structure of the *Pnma* space group (a = 5.193 Å, b = 3.099 Å, c = 5.792 Å), referenced from the COD database under reference code 01-078-1443.

Similarly, the Ni foam was identified as having a cubic structure with a space group of $Fm\bar{3}m$ (reference code 00-001-1260). The diffraction peaks at 2θ values of 52.29°, 61.094°, and 92.336° were attributed to the (111), (200), and (220) planes, respectively. The sharpness and intensity of the peaks indicate a high degree of crystallinity for both Fe and Ni foams. The phosphorisation of Ni foam resulted in the formation of two crystalline phosphide phases: Ni_2P and $Ni_{12}P_5$. The Ni_2P diffractogram was composed of reflections at 47.7°, 55.4°, and 63.9°, corresponding to the (111), (210), and (300) planes, with a hexagonal crystal structure, $P\bar{6}2m$ (a = 6.859 Å, b = 5.859 Å, c = 3.382 Å), identified from the COD database under reference code 01-074-1385. The $Ni_{12}P_5$ phase, with a tetragonal structure and space group $I4/m$ (a = 8.646 Å, b = 8.646 Å, c = 5.07 Å), was identified by reflections at 45.1°, 55.28°, and 57.63°, attributed to the (112), (240), and (312) planes, respectively.

X-ray photoelectron spectroscopy (XPS) was employed to analyse the surface composition and verify the formation of phosphides on metal foams. The results are depicted in Fig. 2. The XPS survey spectra reveal the presence of Fe 2p, Ni 2p, P 2p, C 1s, and O 1s signals, along with minor impurities. The detected oxygen content is primarily attributed to surface oxidation due to air exposure.

In the Fe $2p_{3/2}$ region, 709–712 eV peaks correspond to Fe^{2+} and Fe^{3+}, indicating their bond with oxygen or the presence of phosphates. Meanwhile, the Fe $2p_{3/2}$ peak at 706.7 eV indicates a Fe–P bond. The P $2p_{3/2}$ signal further corroborates the presence of surface phosphides at approximately 129.3 eV. Additionally, the P 2p spectrum includes a peak at 133 eV, characteristic of P–O

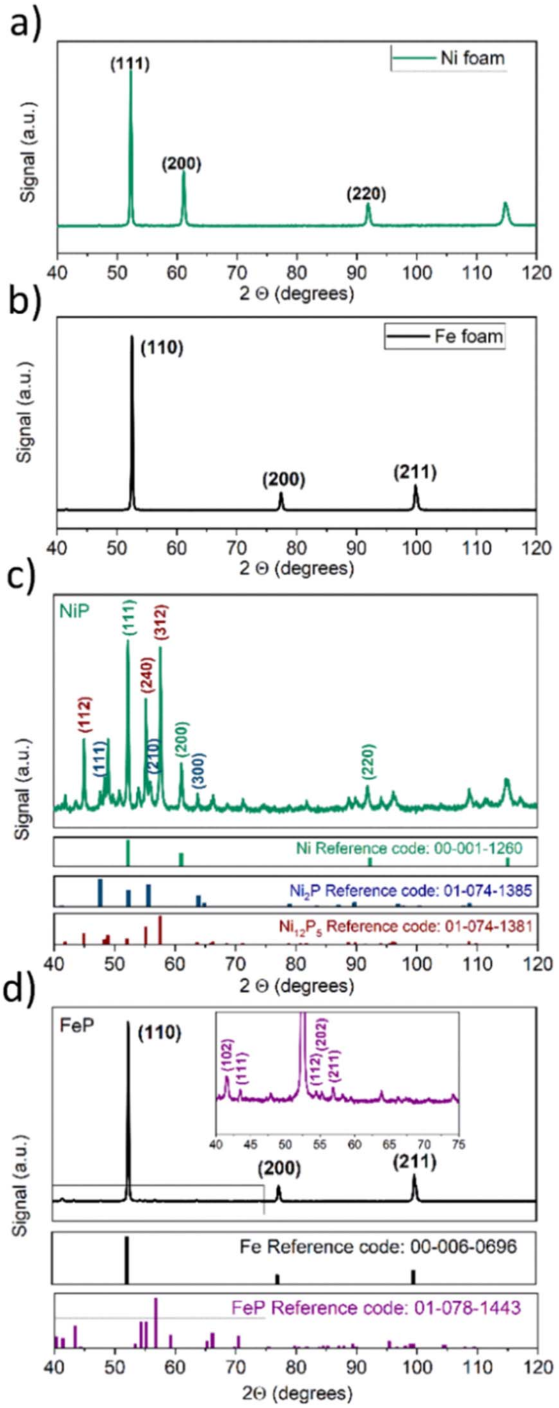

Fig. 1 XRD patterns of (a) pristine Ni foam, (b) pristine Fe foam, (c) Ni foam after phosphorisation, and (d) Fe foam after phosphorisation. Reference patterns for each identified phase are included for comparison.

bonding and suggesting surface oxidation and phosphate formation.

The Ni $2p_{3/2}$ spectrum exhibits Ni^{2+} species, with signals corresponding to NiO at approximately 856.1 eV and nickel hydroxide/phosphate at around 855.7 eV. These signals are accompanied by characteristic satellite features in the 861–866 eV range. A distinct Ni–P peak at approximately 852.7 eV is also evident. The P 2p signal at around 129.6 eV confirms the presence of nickel phosphides. Overall, these findings demonstrate the successful synthesis of a phosphide surface layer on iron and nickel metal foams alongside the presence of surface oxides.

The SEM images of the Fe–P and Ni–P metal foams (Fig. 3) revealed a highly porous, interconnected structure characteristic of the replication method. The porosity was uniform across the samples, with pore size reflecting the original polyurethane foam template. Samples displayed a slightly roughened texture, suggesting the formation of additional surface features beneficial for catalytic activity. EDX analysis confirmed the presence of Fe and Ni as the primary elements, along with P (7.8 wt% in Fe–P and 9.7 wt% in Ni–P), indicating the successful incorporation of P during the phosphorisation process. Additionally, both samples exhibited trace amounts of oxygen, attributed to surface oxidation that occurred during handling or exposure to air.

Electrochemical activity of foam catalysts

The electrocatalytic performance of the Fe–P and Ni–P metal foams was evaluated using polarisation curves and compared to platinum (Pt) as a reference. The results of electrochemical measurements are depicted in Fig. 4 and summarised in Table 2. It should be noted that the polarisation curve of the commercial Pt catalyst in this study exhibits slightly lower activity compared to some previously reported values.[33–37] This variation can be attributed to differences in testing conditions. Nevertheless, the Pt catalyst was employed here as a standard reference under identical conditions to those used for the synthesised materials, ensuring a consistent and meaningful comparison. The polarisation curves revealed that the samples exhibited notable catalytic activity, with Ni–P showing superior performance over Fe–P. Tafel slope analysis provided further insight into the reaction kinetics. The Tafel slopes were 53 mV dec^{-1} for Pt, 79 mV dec^{-1} for Ni–P, and 101 mV dec^{-1} for Fe–P, indicating faster reaction kinetics for Ni–P compared to Fe–P. These results emphasise the superior catalytic efficiency of Ni–P foam compared to Fe–P, consistent with its lower overpotentials across all measured current densities. Additionally, the electrochemical double-layer capacitance (C_{dl}) was determined for both samples to estimate their electrochemically active surface area. The C_{dl} values were 16.2 mF cm^{-2} for Fe–P and 41.8 mF cm^{-2} for Ni–P, reflecting a significantly higher active surface area for the Ni–P sample. The increased surface area of the material resulted in improved catalytic activity and lower overpotential.

To gain insight into the charge transfer characteristics of the catalysts, EIS measurements were performed at a potential of −1.4 V. As shown in Table 3 and Fig. 6, the Nyquist plots reveal a small semicircle in the high-frequency region, indicating a low polarisation resistance. The fitted R_p value of less than 1.8 Ω for both samples confirms the favourable electron transport kinetics, which contribute to the observed catalytic performance. The slightly lower solution resistance observed for Fe–P (1.81 Ω) compared to Ni–P (2.70 Ω) may stem from differences in electrode morphology, surface roughness, or interface quality

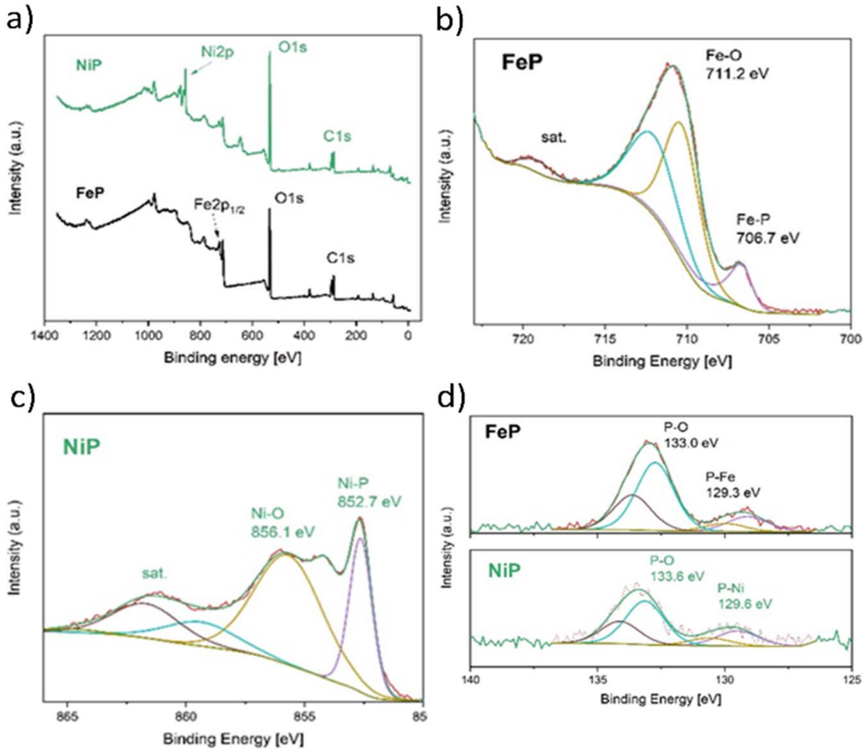

Fig. 2 XPS analysis of synthesized phosphides: (a) survey spectra of Ni–P and Fe–P, (b) high-resolution Fe 2p spectrum of FeP, (c) high-resolution Ni 2p spectrum of NiP, and (d) high-resolution P 2p spectra of FeP and NiP.

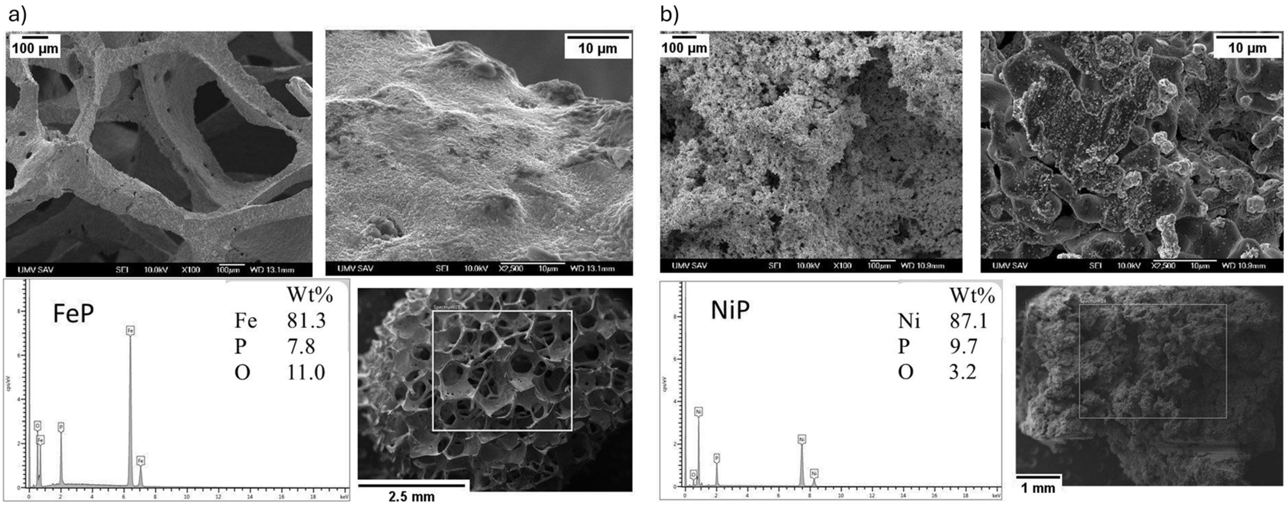

Fig. 3 SEM images and EDX elemental analysis of phosphorised metal foams: (a) FeP and (b) NiP. The micrographs show surface morphology at different magnifications, and corresponding EDX spectra with elemental composition (wt%) confirm the presence of Fe/Ni, P, and O.

with the electrolyte, which can influence ion accessibility and wetting behaviour during measurement.

A combination of polarisation curves, Tafel slopes, and C_{dl} measurements reveals that Ni–P exhibits superior electrocatalytic activity compared to Fe–P, suggesting it is a more efficient electrocatalyst for the water-splitting reaction.

The durability of the catalysts was assessed *via* chronoamperometry over a continuous 24-hour period. As shown in Fig. 6, the current density remained stable with negligible fluctuation, indicating excellent operational stability under alkaline conditions. This result supports the claim of good long-term performance and resistance to degradation during prolonged electrolysis. SEM analysis performed after the stability test (Fig. 6) revealed no significant morphological changes to the catalyst surface, with only minor irregularities observed, likely caused by gas bubble formation and detachment during electrolysis.

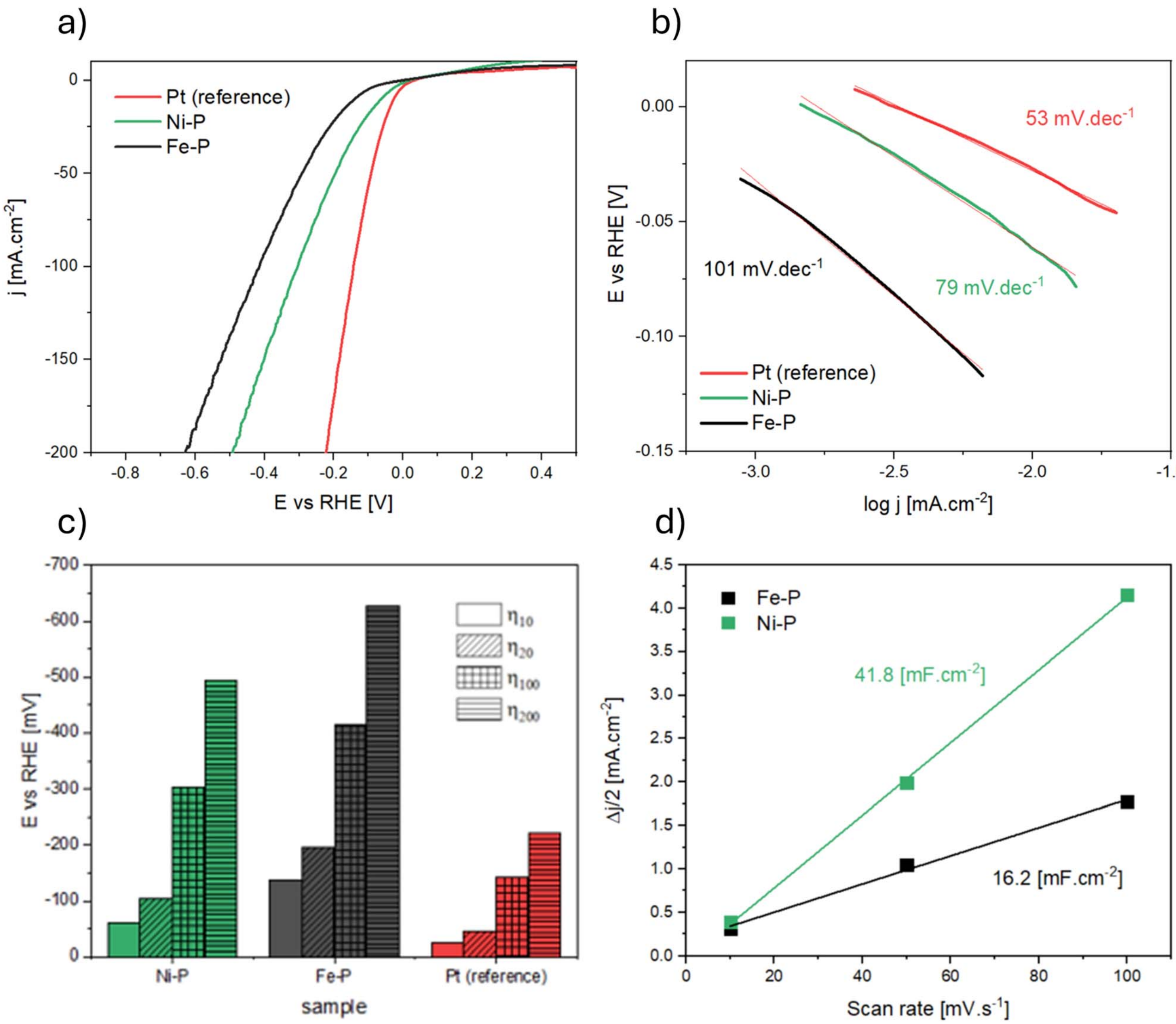

Fig. 4 Electrocatalytic performance of Ni–P and Fe–P compared to Pt in 1 M KOH: (a) polarisation curves measured on a rotating disk electrode (RDE) at a scan rate of 1 mV s^{-1}, (b) corresponding Tafel slopes, (c) comparison of overpotentials required to reach current densities of 10, 20, 100, and 200 mA cm^{-2}, and (d) double-layer capacitance (C_{dl}) derived from scan rate-dependent measurements.

Table 2 Overpotentials (η) at current densities 10, 20, 100, and 200 mA cm^{-2}, Tafel slope values of Fe–P and Ni–P samples, and Pt reference

Sample	η_{10} [mV]	η_{20} [mV]	η_{100} [mV]	η_{200} [mV]	b [mV dec^{-1}]
Ni–P	61	104	304	494	79
Fe–P	138	197	414	628	101
Pt (ref.)	25	46	142	221	53

Optimisation of Ni and Fe unit cells

Initially, the structural properties of the bulk Ni and Fe crystal structures were calculated. The cubic unit cells of Ni and Fe, belonging to the $Fm\bar{3}m$ and $Im\bar{3}m$ space groups, were optimised (Fig. S1†). Ni is coordinated with twelve equivalent Ni atoms, resulting in a composite structure characterised by corner, edge, and face-sharing $NiNi_{12}$ cuboctahedra. The optimised lattice parameter $a = b = c$ is equal to 3.52 Å with a magnetic moment for each Ni atom equal to 0.66 μ_B. On the other hand, Fe is coordinated in a body-centered cubic arrangement, forming bonds with eight equivalent iron atoms. In case of Fe the optimised lattice parameter $a = b = c$ is equal to 2.83 Å with

Table 3 EIS parameters for Ni–P and Fe–P samples obtained in 1 M KOH[a]

			CPE		
Sample	R_s [Ω]	R_p [Ω]	Y_0 [mΩ s^N]	N	χ^2
Ni–P	1.81	1.78	40.8	0.742	0.037
Fe–P	2.70	1.79	2.49	0.719	0.033

[a] CPE – Constant phase element, χ^2 – indicates an error in EIS fit.

Table 4 Calculated lattice parameters, unit cell volumes, magnetic moments (m_s), and bulk energies (E_{bulk}) for optimized Ni and Fe structures

	Lattice parameters				
Structure	$a = b = c$	$\alpha = \beta = \gamma$	Volume [Å^3]	m_s [μ_B]	E_{bulk} [eV]
Ni	3.517	90.000	43.503	0.662	−18.682
Fe	2.833	89.997	22.737	2.244	−6.812

a magnetic moment for each Fe atom equal to 2.24 μ_B. All optimised lattice parameters with calculated magnetic moments are summarised in Table 4.

Adsorption of H atom on Ni surfaces

To study the adsorption of hydrogen atoms, it was first necessary to analyse the adsorption of P atoms on the Ni(111) surface and Fe(110) surface with a defect. The prepared Ni(111) and Ni(111) surfaces are displayed in Fig. S2.† The resulting structures with possible adsorption sites are depicted in Fig. 5, summarising the E_{ads} and ΔG_{H^*} in Table 5. The adsorption of the P atom occurred on the F site of the Ni(111) surface with E_{ads} equal to −2.70 eV. The P atom was bonded to 3 Ni atoms with bond lengths of ∼2.13 Å. Regarding the adsorption of the P atom at defect of Ni(111) surface, the E_{ads} was equal to −4.13 eV with symmetric alignment represented by the similar size of 6 Ni–P bond lengths ∼2.45 Å of Ni atoms in the top layer and 3 Ni–P bond lengths ∼2.36 Å of Ni atoms in the second layer.

Subsequently, the adsorption of the H atom was studied by DFT calculations on the Ni(111) surface, Ni(111)P$_{ads}$ – surface with P adsorbed to the F site and Ni(111)P$_{def}$ – surface with P adsorbed to the defect. The optimised structures are displayed in Fig. 6, along with corresponding values of E_{ads}, ΔG_{H^*} and structural parameters outlined in Table 5. When applying the H atom on the Ni(111) surface, the H atom is adsorbed to the H site with E_{ads} of −0.66 eV and three symmetric bonds occurring between Ni1–P, Ni2–P and Ni3–P with bond lengths of ∼1.71 Å. With Ni(111)P$_{ads}$ surface, the H atom adsorbed to the T site of the P atom with E_{ads} of −0.239 eV, while with Ni(111)P$_{def}$ surface, the H atom adsorption also occurred on the T site of the P atom. However, the E_{ads} was higher with a positive value of 0.44 eV. This suggests that the adsorption of the H atom in this configuration does not occur.

Consequently, the ΔG_{H^*} values have been calculated for all Ni(111) surfaces with adsorbed H atoms. Values are displayed in Fig. 7). According to these results, ΔG_{H^*} is lowest with a Ni(111) surface with a value of −0.41 eV and closest to the ideal state with a Ni(111)P$_{ads}$ surface with a value of 0.01 eV. The Ni(111)P$_{def}$ surface leads to the highest ΔG_{H^*} value of 0.69 eV, which is unsuitable for HER. The surfaces can be ordered according to their ΔG_{H^*} from lowest to highest value as follows: Ni(111)P$_{ads}$ < Ni(111) < Ni(111)P$_{def}$.

Additionally, other possible structures with an H atom adsorbed to a Ni atom instead of a P atom are displayed in Fig. S3 and S4† with corresponding E_{ads}, ΔG_{H^*} and structural parameters in Table S1.† H adsorption on Ni(111)P$_{ads}$ and Ni(111)P$_{def}$ can occur at four additional sites in both cases, namely at the H$_1$, F$_1$, H$_2$, and F$_2$ sites. ΔG_{H^*} depicted in Table S1† show a decreasing value with the H atom adsorbed further away from the P atom.

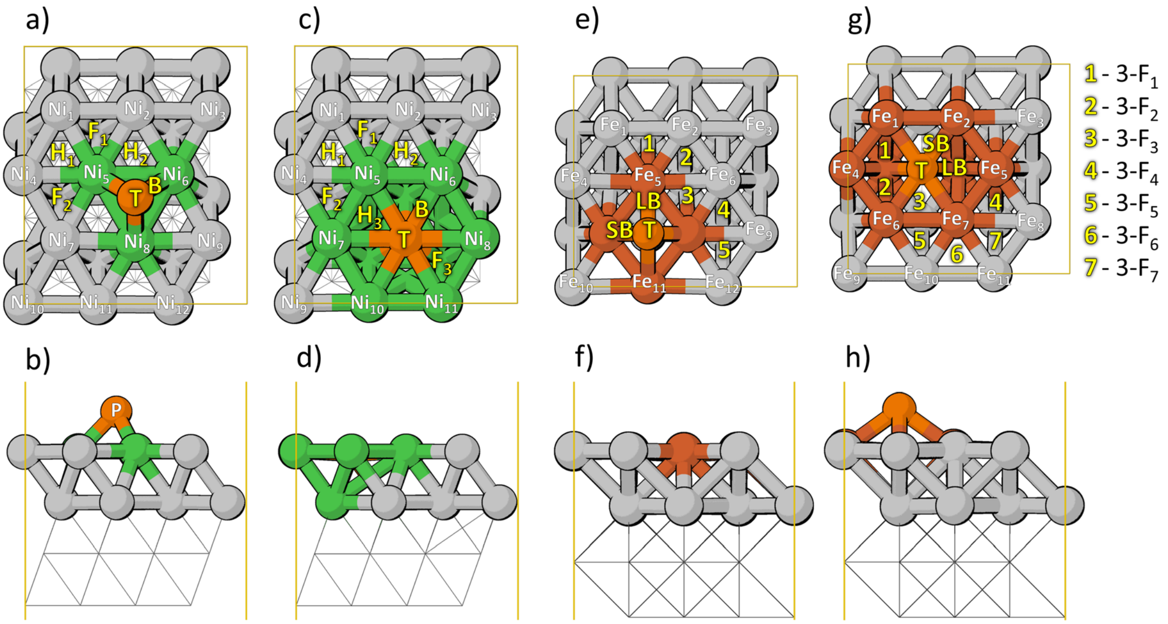

Fig. 5 Optimized Ni(111) surfaces with a P atom adsorbed at the (a and b) F site and (c and d) D site, shown in top and side views, respectively; and optimized Fe(110) surfaces with a P atom adsorbed at the (e and f) F site and (g and h) D site, also shown in top and side views, respectively. Yellow letters indicate possible hydrogen adsorption sites: B – bridge, F – fcc hollow, H – hcp hollow, T – top, 3-F – 3-fold, LB – long bridge, and SB – short bridge.

Table 5 Values of adsorption energies (E_{ads}), Gibbs free energies (ΔG_{H^*}) and structural parameters for adsorbed H on different Ni and Fe surfaces

Atom	Surface	Adsorption site	E_{ads} [eV]	ΔG_{H^*} [eV]	$d_{surf\text{-}ads}$ [Å]
P	Ni(111)	F	−2.703	—	Ni_1–P: 2.129 Ni_2–P: 2.136 Ni_3–P: 2.134
	Ni(111)	D	−4.133	—	Ni_1–P: 2.488 Ni_2–P:2.488 Ni_3–P: 2.466 Ni_4–P: 2.455 Ni_5–P: 2.455 Ni_6–P: 2.466 Ni_7–P: 2.356 Ni_8–P: 2.356 Ni_9–P: 2.357
H	Ni(111)	H	−0.656	−0.406	Ni_1–H: 1.712 Ni_2–H: 1.712 Ni_3–H: 1.711
	Ni(111)P_{ads}	T	−0.239	0.011	P–H: 1.429
	Ni(111)P_{def}	T	0.439	0.689	P–H: 1.447
P	Fe(110)	LB	−3.372	—	Fe_1–P: 2.412 Fe_2–P: 2.175 Fe_3–P: 2.411 Fe_4–P: 2.173
	Fe(110)	D	−4.133	—	Fe_1–P: 2.380 Fe_2–P: 2.371 Fe_3–P: 2.814 Fe_4–P: 2.369 Fe_5–P: 2.378 Fe_6–P: 2.874 Fe_7–P: 2.750 Fe_8–P: 2.343 Fe_9–P: 2.755 Fe_{10}–P: 2.362
H	Fe(110)	3-F	−1.565	−1.315	Fe_1–H: 0.177 Fe_2–H: 0.178 Fe_3–H: 0.179
	Fe(110)P_{ads}	T	−0.105	0.145	P–H: 0.143
	Fe(110)P_{def}	T	0.686	0.936	P–H: 1.45

As indicated by these results, adding P atoms and their location on the Ni(111) surface can significantly affect the resulting value of E_{ads} and ΔG_{H^*}. HER will be favoured on the Ni(111) surface with a suitable amount of adsorbed P atoms, leading to weaker binding of the H atom and easier cleavage from the surface for H_2 formation.

Adsorption of H atom on Fe surfaces

Similarly, the analysis of P atom adsorption was also conducted on the Fe(110) surface and the Fe(110) surface with a defect (Fig. S2†). The adsorption on the Fe(110) surface occurred on the LB site with E_{ads} equal to −2.91 eV. P atom bonded to the surface symmetrically through 4 Fe atoms with bond lengths of ~2.17 Å and ~2.41 Å. When the P atom was applied to the defect of Ni(111) surface, the value of E_{ads} decreased to −4.13 eV with P being bonded symmetrically to the surface through 6 Fe atoms in the top layer with bond lengths ~2.37 and ~2.38 Å and 4 Fe atoms in a second layer with bond lengths 2.75 and ~2.35 Å.

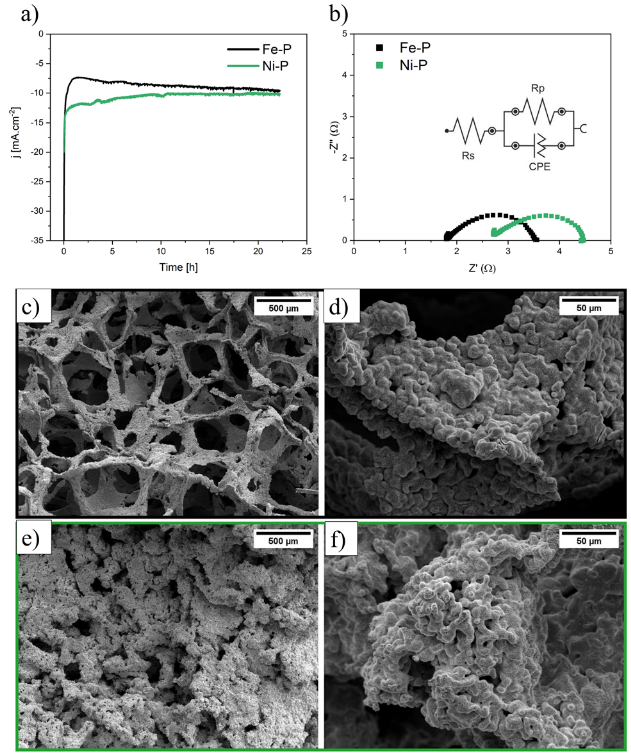

Fig. 6 Electrochemical and structural stability analysis of Fe–P and Ni–P. (a) Chronopotentiometry curves showing long-term HER stability at a constant current density in 1 M KOH. (b) Nyquist plots obtained from electrochemical impedance spectroscopy (EIS) for Fe–P and Ni–P; inset shows the equivalent circuit model used for fitting, including solution resistance (R_s), polarisation resistance (R_p), and constant phase element (CPE). SEM images of (c and d) Fe–P and (e and f) Ni–P foams at low and high magnifications, respectively, obtained after stability tests.

Eventually, H atom adsorption was considered using DFT calculations on the Fe(110) surface, Fe(110)P_{ads} – surface with P adsorbed to the 3-F site and Fe(110)P_{def} – surface with P adsorbed to the defect. Fig. 6 illustrates the optimised structures, while Table 5 provides the relevant values for E_{ads}, ΔG_{H^*} and the corresponding structural parameters.

The adsorption of an H atom on the Fe(110) surface occurs at the 3-F site, with an associated adsorption energy of −1.57 eV. This interaction is characterised by the formation of four symmetric bonds between Fe_1–P, Fe_2–P, Fe_3–P and Fe_4–P, with bond lengths measuring ~2.41 Å and ~2.17 Å. On the Fe(110)P_{ads} surface, the H atom adsorption occurs at the T site of the P atom, resulting in E_{ads} of −0.105 eV. On the Fe(110)P_{def} surface, the hydrogen atom also adsorbs at the T site of the P atom. However, the E_{ads} is significantly higher, with a positive value of 0.69 eV, resembling the behaviour on the Ni(111)P_{def} surface.

The ΔG_{H^*} values for all Fe(110) surfaces with adsorbed H atoms have been computed and are presented in Fig. 7. The results reveal that the Fe(110) surface has the lowest ΔG_{H^*} value of −1.32 eV, while the Fe(110)P_{ads} is closer to ideal state with ΔG_{H^*} value of 0.15 eV. The Fe(110)P_{def} surface exhibits the highest value of ΔG_{H^*} 0.94 eV, which is even more incompatible with the HER process. In summary, the Fe surfaces can be

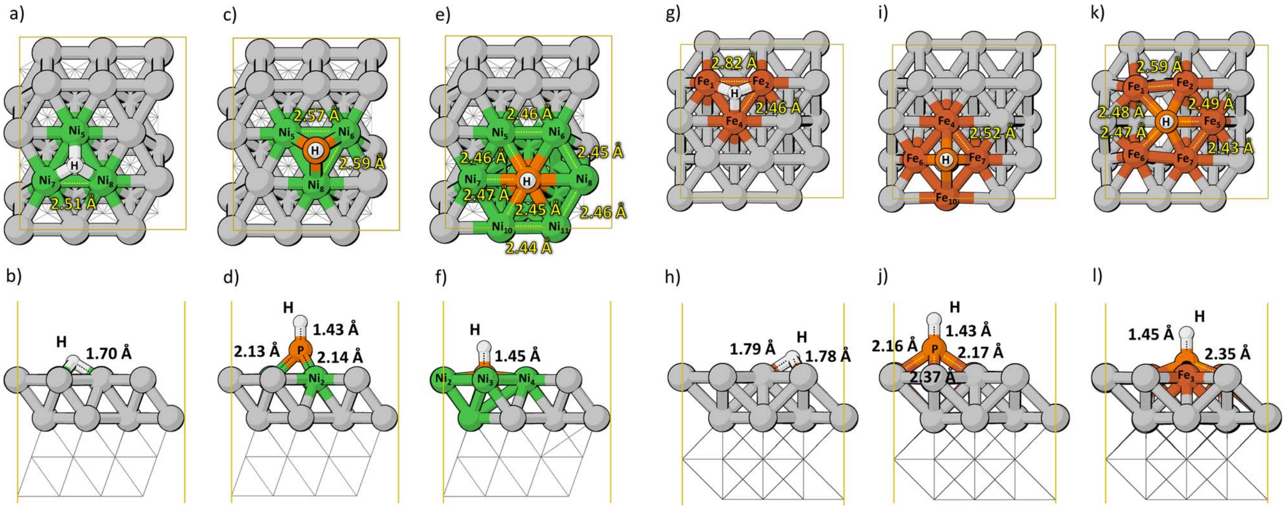

Fig. 7 Optimized Ni(111) and Fe(110) surfaces with adsorbed H atoms. (a and b) H adsorbed at the H site on Ni(111), (c and d) H adsorbed at the top (T) site of a P atom on Ni(111), (e and f) H adsorbed at the T site of a P atom in a defect on Ni(111); (g and h) H adsorbed at the 3-fold (3-F) site on Fe(110), (i and j) H adsorbed at the T site of a P atom on Fe(110), and (k and l) H adsorbed at the T site of a P atom in a defect on Fe(110). Top and side views are shown for each configuration.

arranged in order of increasing $\Delta G_{\mathrm{H}*}$ values as follows: Fe(110) $\mathrm{P_{ads}}$ < Fe(110) < Fe(110)$\mathrm{P_{def.}}$ Similar behaviour can be observed when comparing the adsorption of the H atom on Ni and Fe surfaces. The closest $\Delta G_{\mathrm{H}*}$ values to the ideal state for H atom cleavage from given surfaces are in the case of Ni(111)$\mathrm{P_{ads}}$ and Fe(110)$\mathrm{P_{ads}}$. Covering the surfaces with P atoms leads to an increase in $\Delta G_{\mathrm{H}*}$ towards the ideal value.

All other possible structures with an H atom adsorbed to a Fe atom instead of a P atom are displayed in Fig. S3 and S4,† along with corresponding E_{ads}, $\Delta G_{\mathrm{H}*}$ and structural parameters in Table S1.† Additional H adsorption on Fe(110)$\mathrm{P_{ads}}$ occurs at the 3-$\mathrm{F_1}$, 3-$\mathrm{F_2}$, $\mathrm{H_2}$, and 3-$\mathrm{F_5}$ sites. On Fe(110)$\mathrm{P_{def}}$ other possible H adsorption sites include 3-$\mathrm{F_5}$, 3-$\mathrm{F_6}$ and 3-$\mathrm{F_7}$ sites. Also in these cases, the closer to the P atom the H adsorbs on the Fe surface, the higher the value of $\Delta G_{\mathrm{H}*}$.

In all cases, the Ni surfaces yield better ΔGH* values compared to Fe surfaces, closer to the ideal state for HER. This corresponds with experimental values obtained for Ni–P samples and explains the superior catalytic activity of the prepared Ni samples.

Experimental

Chemicals and preparation of the Ni and Fe catalysts

Iron and nickel metal catalysts in foams were prepared using the replication method. This method was adapted from Gubóová *et al.*[27] to achieve the desired structural and catalytic characteristics of the metal foams. Briefly, iron powder (<10 μm, 99.9%, Alfa Aesar) and nickel powder (<50 μm, 99.7%, Sigma Aldrich) were used as starting materials, with gelatin (Acros Organics) dissolved in distilled water serving as the binder. Polyurethane foam, employed as a template, was immersed in the prepared slurry to ensure thorough coating. The excess slurry was removed by compression, and the coated foam was dried at 200 °C to maintain structural integrity.

The dried samples underwent a two-step sintering process. Initially, they were sintered in a nitrogen atmosphere at 450 °C for 2 hours to remove the polyurethane template and binder material. This was followed by sintering in a reducing atmosphere at 1200 °C for 1 hour, which promoted the consolidation of metal particles and the formation of a porous metal structure.

A phosphorisation step was performed to enhance the catalytic properties of the metal foams. The process was adapted from ref. 38 and involved temperature/programmed reduction in a hydrogen atmosphere. In more detail, the metal foams were

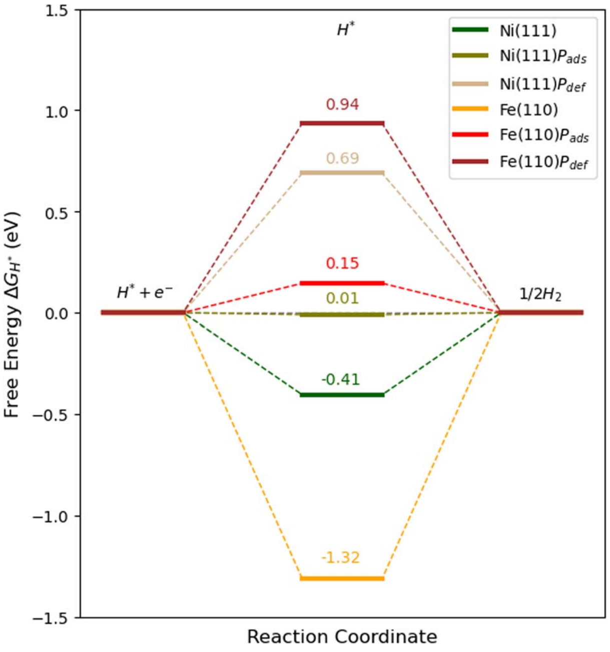

Fig. 8 Gibbs free energy diagram ($\Delta G_{\mathrm{H}*}$) for hydrogen adsorption on various Ni(111) and Fe(110) surfaces, including pristine, adsorbed P ( ), and P adsorbed in defect ($\mathrm{P_{def}}$) configurations.

first cleaned using an ultrasonic bath with acetone, hydrochloric acid, ethanol, and distilled water, and then dried at room temperature. Subsequently, they were placed on the ceramic boat. In contrast, another ceramic boat filled with sodium hypophosphite monohydrate (>99%, Biotech), used as the phosphorus source, was placed in the furnace in front of the boat containing the sample along the gas stream. The furnace was heated to 300 °C at a rate of 1 °C min^{-1} and maintained at the desired temperature for 2 hours. Samples were then cooled to room temperature. This process facilitated the incorporation of phosphorus into the metal structure, yielding Fe–P and Ni–P with improved functional properties (Fig. 8).

Catalyst characterisation

The crystalline phases of the Fe and Ni foams were identified using X-ray diffraction (XRD) using a PhilipsX' PertPro diffractometer. The XRD patterns were recorded using a Co Kα radiation source over a 2θ range of 40° to 120°. The diffraction patterns were analysed to verify the samples' overall crystalline structure.

After the phosphorisation treatment, the morphology and elemental composition of the prepared samples were analysed using a scanning electron microscope (JSM-7000F, JEOL, Japan) coupled with energy-dispersive X-ray spectroscopy (Oxford Instruments, England). SEM was employed to observe the surface structure and porosity of the metal foams, while EDX provided elemental mapping and confirmed the phosphorus distribution after the phosphorisation process.

X-ray photoelectron spectroscopy (XPS) analysis was performed using a Thermo Scientific Nexsa G2 Surface Analysis System (Thermo Fisher Scientific, UK), equipped with a micro-focused, monochromatic Al Kα X-ray source, to confirm phosphide formation.

Electrochemical characterisation

The electrocatalytic performance of the phosphorised Fe and Ni metal foams was evaluated in a three-electrode configuration using 1 M KOH as the electrolyte. The working electrode consisted of a prepared metal foam that was directly immersed in the electrolyte. A platinum foil served as the counter electrode, and a saturated calomel electrode (SCE) was used as the reference electrode.

Electrochemical measurements were conducted using a potentiostat PGSTAT302 N (Metrohm Autolab, Netherlands). Polarisation curves were obtained by linear sweep voltammetry (LSV) at a scan rate of 1 mV s^{-1}, ranging from 0.3 V to −1.5 V. The Tafel slopes were calculated from the polarisation curves to evaluate the kinetics of the catalytic reactions.

The electrochemical double-layer capacitance (C_{dl}) was estimated using cyclic voltammetry (CV) measurements. CV was performed at open-circuit potential (OCP) with varying scan rates (10, 50, 100 mV s^{-1}) over a 100 mV range near the open-circuit potential (OCP) to ensure measurements were performed in the non-faradaic region. The capacitive current was plotted as a function of the scan rate to determine the C_{dl}, which indicates the electrochemically active surface area (ECSA).

Current densities were normalised using the electrochemically active surface area determined from the C_{dl}. The ECSA was calculated using the following equation:

$$\text{ECSA} = \frac{C_{\text{dl}}}{C_{\text{s}}} \tag{4}$$

where C_{dl} is the measured double-layer capacitance, and C_{s} represents the specific capacitance of the electrode. For most transition metals in 1 M KOH, C_{s} is typically reported as 0.040 mF cm^{-2}.[39]

All recorded potentials were recalculated to the reversible hydrogen electrode (RHE) scale using the formula:

$$E_{\text{RHE}} = E_{\text{SCE}} + 0.059 \times \text{pH} + 0.244 \tag{5}$$

Electrochemical Impedance Spectroscopy (EIS) measurements were performed in 1 M KOH at an applied potential of −1.4 V, with a frequency range of 100 kHz to 0.1 Hz and an amplitude of 5 mV. The Nyquist plots were fitted using an equivalent circuit model to estimate the solution and polarisation resistance. The long-term stability of the catalysts was evaluated using chronoamperometry at a constant potential −1.2 V for 24 hours in 1 M KOH. After the stability tests, SEM analysis was performed on the electrodes to evaluate possible morphological changes.

All experiments were conducted at room temperature, and each measurement was repeated several times to ensure reproducibility and reliability of the data. The representative curve was then selected.

Computational methodology

Spin-polarised density functional theory (DFT) calculations were performed using the Quantum ESPRESSO suite, employing the Plane-Wave (PW) basis set and Ultrasoft (US) pseudopotential (PP) approach. The calculations were performed using the Plane-Wave Self-Consistent Field (PWscf) code.[40,41] The Kohn–Sham equations were solved using the Perdew–Burke–Ernzerhof (PBE) exchange–correlation functional within the generalised gradient approximation (GGA).[42] The kinetic energy cutoff values were set to 45 Ry for wave functions and 360 Ry for charge density. A Gaussian smearing value of 0.003 Ry was applied to facilitate self-consistent field (SCF) convergence, with a convergence threshold set at 10^{-6} Ry. The Ni(111) and Fe(110) surfaces were constructed based on the optimised Ni and Fe unit cells, with lattice parameters and surface sites corresponding to crystallographic data obtained from X-ray diffraction analysis of experimentally synthesised samples. The Ni(111) and Fe(110) surface models consisted of 47 nickel (Ni) atoms and 48 iron (Fe) atoms organised as periodically repeating four-layer slabs within a (3 × 4) orthogonal unit cell configuration (Fig. S2a, b, d and e†). The defective Ni(111) and Fe(110) surfaces (Fig. S2c and f†) were prepared by removing one Ni and Fe atom from the surface and subsequently optimising the defective Ni(111) and Fe(110). The bottom layers were fixed during optimisation to allow structural relaxation of the top two atomic layers. A vacuum region of 15 Å was introduced on both sides of the slab to prevent interactions between periodic images. Monkhorst–Pack *k*-point grids of 9 × 9 × 9 and 8 × 8 × 1 were utilised for the unit cell and surface calculations, respectively.

Subsequently, P and H atoms were applied to different adsorption sites on Ni(111) and Fe(110) surfaces, namely 3-F – 3-fold, B – bridge, D – defect, F – fcc hollow, H – hcp hollow, and T – top. To calculate the adsorption energy, ΔE_H, eqn (6) was employed:

$$\Delta E_H = E_{S+H} - \left(E_S + \frac{1}{2}E_{H_2}\right) \tag{6}$$

E_{S+H} is the total energy of the adsorbate-substrate system; E_S is the energy of an uncovered surface, and E_H is the energy of the adsorbed H atom.

The Gibbs free energy of hydrogen adsorption, ΔG_{H^*}, was calculated using the computational hydrogen electrode method of Nørskov *et al.*,[43] represented by the following equation (eqn (7)):

$$\Delta G_{H^*} = \Delta E_{S+H} + \Delta E_{ZPE} - T\Delta S_H \tag{7}$$

where ΔE_H is the calculated adsorption energy, ΔE_{ZPE} is the difference in zero-point energy of hydrogen in the adsorbed state and the gas phase, and ΔS_H is the entropy difference between the adsorbed state and the gas phase of hydrogen at standard conditions (atmospheric pressure, 298 K). The value of ΔE_{ZPE} for hydrogen adsorption on different metallic surfaces was set to 0.04 eV, and at 298 K, the Gibbs free energy of adsorbed hydrogen can be presented as $\Delta G_{H^*} = \Delta E_{S+H} + 0.24$, according to the study of Nørskov *et al.*[43]

Limitations of the computational model

Our DFT model uses ideal Ni(111) and Fe(110) surfaces based on XRD-derived lattice parameters, which simplifies the real catalyst morphology. While we included single-atom defects to approximate undercoordinated sites, the complex surface features of the foam, such as grain boundaries, mixed facets, or oxidised/phosphated layers, were not explicitly modelled due to computational constraints.

Spin-polarised calculations were used to capture magnetic effects, but DFT+U was not applied, as standard GGA-PBE is generally adequate for metallic and phosphidic systems. However, for oxidised surfaces, DFT+U may be necessary and will be considered in future work.

Finally, the computational hydrogen electrode approach does not account for solvent or electrochemical interface effects, which may influence ΔG_{H^*} under real HER conditions.

Conclusions

This study demonstrates the superior catalytic activity of the Ni–P catalyst compared to the Fe–P catalyst, highlighting the synergy between Ni and phosphorus for efficient hydrogen evolution reaction (HER). Experimental findings confirmed the successful incorporation of P into both catalysts, with Ni–P showcasing higher catalytic performance attributed to its optimised binding properties.

Polarisation curves revealed that Ni–P required significantly lower overpotentials to achieve even high current densities of 200 mA cm^{-2} (494 mV) compared to Fe–P (628 mV). Tafel slope analysis further confirmed the faster reaction kinetics of Ni–P (79 mV dec^{-1}) compared to Fe–P (101 mV dec^{-1}). Electrochemical double-layer capacitance measurements revealed a larger electrochemically active surface area for Ni–P (41.8 mF cm^{-2}) compared to Fe–P (16.2 mF cm^{-2}). An expanded active surface area in Ni–P enhanced HER activity due to increased accessibility of active sites for hydrogen evolution.

DFT calculations provided valuable insight into the adsorption behaviour of P and H atoms on the Ni(111) and Fe(110) surfaces, both pristine and with defects. A comparison of H atom adsorption on Ni and Fe surfaces indicates a similar behaviour. The ΔG_{H^*} values that approach the ideal value for the cleavage of H atoms from these surfaces are found in Ni(111)P$_{ads}$ and Fe(110)P$_{ads}$ with 0.01 eV and 0.15 eV, respectively. Covering these surfaces with P atoms increases ΔG_{H^*} and approaches the ideal value that promotes HER. On the other hand, the integration of P into the Ni and Fe surfaces leads to a significant increase in E_{ads} (0.44 and 0.69 eV) and ΔG_{H^*} (0.69 and 0.94 eV), which does not allow H atom adsorption and subsequent cleavage and therefore is unfavourable for the hydrogen evolution reaction (HER). This observation is consistent with experimental data obtained from Ni–P and Fe–P samples, explaining the superior catalytic activity observed in the prepared Ni–P samples for HER.

Overall, the findings highlight the crucial role of phosphorus in regulating the electronic and structural properties of transition metal surfaces and establish the significant impact of P incorporation and its spatial configuration on the catalytic properties of Ni and Fe surfaces. The findings suggest that tailoring the amount and distribution of P on metal surfaces can significantly enhance HER performance by promoting optimal hydrogen adsorption and desorption dynamics. The results pave the way for the rational design of transition metal-based catalysts with tailored compositions and surface structures to enhance energy conversion processes, particularly for alkaline water splitting.

Data availability

The data supporting this article have been included as part of the ESI.†

Author contributions

N. Podrojková: data curation, investigation, methodology, visualization, writing – original draft, A. Gubóová: data curation, investigation, methodology, visualization, writing – review & editing, M. Streckova: writing – review & editing, F. Kromka: methodology, investigation, R. Oriňaková: writing – review & editing.

Conflicts of interest

The authors declare no competing financial interest.

Acknowledgements

This work was supported by the EU NextGenerationEU through the Recovery and Resilience Plan for Slovakia under the project no. 09I03-03-V04-00109, the Slovak Research and Development Agency (project APVV-20-0299) and the Scientific Grant Agency of the Ministry of Education, Science, Research and Sport of the Slovak Republic (project VEGA 1/0057/25). Part of the research results were obtained using the computational resources procured in the national project National Competence Centre for high-performance Computing (project code: 311070AKF2) funded by the European Regional Development Fund, EU Structural Funds Informatization of Society, Operational Program Integrated Infrastructure.

Notes and references

1 D. Li, Z. Guo, R. Zhao, H. Ren, Y. Huang, Y. Yan, W. Cui and X. Yao, *J. Colloid Interface Sci.*, 2024, **653**, 1725–1742.
2 A. S. Emam, M. O. Hamdan, B. A. Abu-Nabah and E. Elnajjar, *Int. J. Hydrogen Energy*, 2024, **64**, 599–625.
3 A. Loh, X. Li, O. O. Taiwo, F. Tariq, N. P. Brandon, P. Wang, K. Xu and B. Wang, *Int. J. Hydrogen Energy*, 2020, **45**, 24232–24247.
4 Q. Guo, J. Mao, J. Huang, Z. Wang, Y. Zhang, J. Hu, J. Dong, S. Sathasivam, Y. Zhao, G. Xing, H. Pan, Y. Lai and Y. Tang, *Small*, 2020, **16**, 1–9.
5 P. Zhou, D. Liu, Z. Wen, M. Chen, Q. Liu, Y. Ke, S. Li, S. Chen, C. T. Kwok, S. Wang, Y. Tang and H. Pan, *Int. J. Hydrogen Energy*, 2021, **46**, 18878–18886.
6 C. Xu, Y. Hong, Z. Li, X. Di, W. Wang, X. Dong and X. Mou, *Coord. Chem. Rev.*, 2025, **523**, 216287.
7 N. Esfandiari, M. Aliofkhazraei, A. N. Colli, F. C. Walsh, S. Cherevko, L. A. Kibler, M. M. Elnagar, P. D. Lund, D. Zhang, S. Omanovic and J. Lee, *Prog. Mater. Sci.*, 2024, **144**, 101254.
8 S. Liu, Y. Wei, M. Wang and Y. Shen, *Coord. Chem. Rev.*, 2025, **522**, 216190.
9 S. Dash, A. S. K, J. S, V. H. W. D, E. D, S. K. Surapraraju and S. K. Natarajan, *Int. J. Hydrogen Energy*, 2024, **83**, 614–629.
10 H. M. Zhang, J. J. Wang, Y. Meng and J. Sun, *Int. J. Hydrogen Energy*, 2022, **47**, 36084–36097.
11 A. Raveendran, M. Chandran and R. Dhanusuraman, *RSC Adv.*, 2023, **13**, 3843–3876.
12 J. Zhu, L. Hu, P. Zhao, L. Y. S. Lee and K. Y. Wong, *Chem. Rev.*, 2020, **120**, 851–918.
13 F. Bao, E. Kemppainen, I. Dorbandt, R. Bors, F. Xi, R. Schlatmann, R. van de Krol and S. Calnan, *ChemElectroChem*, 2021, **8**, 195–208.
14 L. Su, S. Zhang, H. Wu, S. Zhou, C. Cui and H. Pang, *Nano Energy*, 2024, **130**, 110177.
15 W. Luo, Y. Yu, Y. Wu, Z. Ma, X. Ma, Y. Jiang, W. Shen, R. He, W. Su and M. Li, *Appl. Catal., B*, 2023, **336**, 122928.
16 L. K. Putri, B. J. Ng, R. Y. Z. Yeo, W. J. Ong, A. R. Mohamed and S. P. Chai, *Chem. Eng. J.*, 2023, **461**, 141845.
17 L. Yang, T. Yang, E. Wang, X. Yu, K. Wang, Z. Du, S. Cao, K. C. Chou and X. Hou, *J. Mater. Sci. Technol.*, 2023, **159**, 33–40.
18 S. Liu, L. Li, T. Yang, E. Wang, X. Yu, Y. Hou, Z. Du, S. Cao, K. C. Chou and X. Hou, *J. Mater. Sci. Technol.*, 2025, **220**, 92–103.
19 A. B. Silva, M. Medina, L. A. Goulart and L. H. Mascaro, *Electrochim. Acta*, 2024, **475**, 143679.
20 S. Battiato, L. Bruno, A. Terrasi and S. Mirabella, *ACS Appl. Energy Mater.*, 2022, **5**, 2391–2399.
21 X. Zhang, Y. He, B. Zhu, X. Wan, S. Hua and H. Tang, *Int. J. Hydrogen Energy*, 2023, **48**, 4686–4693.
22 A. A. Alothman, J. H. Shah, M. Un Nisa, S. Mohammad, A. G. Abid, M. Usman and M. Adnan, *Int. J. Hydrogen Energy*, 2024, **107**, 460–468.
23 J. Zhong, T. Zhang, J. Tian, W. Gao and Y. Wang, *Inorganics*, 2024, **12**, 1–13.
24 L. Qi, Z. Huang, M. Liao, L. Wang, L. Wang, M. Gao, T. Taylor Isimjan and X. Yang, *Chem.–Eur. J.*, 2023, **29**, 1–8.
25 G. Dong, T. Chen, F. Xie, D. Xue, T. Liu, L. Chen, J. Xia, S. Du, F. Wang, F. Xie and J. C. Ho, *J. Alloys Compd.*, 2023, **968**, 171746.
26 D. Li and X. Wu, *Catalysts*, 2024, **14**, 1–9.
27 A. Gubóová, R. Oriňaková, M. Strečková, M. Paračková, O. Petruš, B. Plešingerová and M. Mičušík, *Mater. Today Chem.*, 2023, **34**, 101778.
28 C. Hitz and A. Lasia, *J. Electroanal. Chem.*, 2001, **500**, 213–222.
29 C. Hu, F. Ding, C. Lv, L. Zhou, N. Zeng, A. Liu, J. Cai and T. Tang, *Sep. Purif. Technol.*, 2025, **352**, 128249.
30 X. Zhao, X. Du and X. Zhang, *J. Alloys Compd.*, 2024, **1008**, 176794.
31 X. Y. Zhang, F. T. Li, Z. N. Shi, B. Dong, Y. W. Dong, Z. X. Wu, L. Wang, C. G. Liu and Y. M. Chai, *J. Colloid Interface Sci.*, 2022, **615**, 445–455.
32 T. Cui, J. Chi, J. Zhu, X. Sun, J. Lai, Z. Li and L. Wang, *Appl. Catal., B*, 2022, **319**, 121950.
33 X. Wang, L. Xia, C. Guo, L. L. Luo, J. Dai, X. Liu, L. He, C. Yang, Y. Xu, B. Zeng and L. Dai, *Appl. Surf. Sci.*, 2023, **614**, 156276.
34 Y. Xu, R. Wang, Z. Liu, L. Gao, T. Jiao and Z. Liu, *Green Energy Environ.*, 2022, **7**, 829–839.
35 Y. Zhu, M. Klingenhof, C. Gao, T. Koketsu, G. Weiser, Y. Pi, S. Liu, L. Sui, J. Hou, J. Li, H. Jiang, L. Xu, W. H. Huang, C. W. Pao, M. Yang, Z. Hu, P. Strasser and J. Ma, *Nat. Commun.*, 2024, **15**, 1447.
36 W. Wu, X. Ma, Y. Zhu, F. Hu, G. Huang, N. Wang, S. Ning, Y. Zhu, P. Kang Shen and J. Zhu, *Chem. Eng. J.*, 2023, **478**, 147425.
37 X. Q. Wang, X. Y. Ma, W. Z. Wu, H. B. He, N. N. Wang, R. J. Zheng, S. J. Ma, Y. Q. Zhu, P. K. Shen and J. L. Zhu, *Rare Met.*, 2024, **43**, 1977–1988.
38 J. Xing, Z. Zou, K. Guo and C. Xu, *J. Mater. Res.*, 2018, **33**, 556–567.
39 E. Cossar, M. S. E. Houache, Z. Zhang and E. A. Baranova, *J. Electroanal. Chem.*, 2020, **870**, 114246.
40 P. Giannozzi, O. Andreussi, T. Brumme, O. Bunau, M. B. Nardelli, M. Calandra, R. Car, C. Cavazzoni, D. Ceresoli, M. Cococcioni, *et al.*, *J. Phys.: Condens. Matter*, 2017, **29**, 465901.

41 P. Giannozzi, S. Baroni, N. Bonini, M. Calandra, R. Car, C. Cavazzoni, D. Ceresoli, G. L. Chiarotti, M. Cococcioni, I. Dabo, A. Dal Corso, S. De Gironcoli, S. Fabris, G. Fratesi, R. Gebauer, U. Gerstmann, C. Gougoussis, A. Kokalj, M. Lazzeri, L. Martin-Samos, N. Marzari, F. Mauri, R. Mazzarello, S. Paolini, A. Pasquarello, L. Paulatto, C. Sbraccia, S. Scandolo, G. Sclauzero, A. P. Seitsonen, A. Smogunov, P. Umari and R. M. Wentzcovitch, *J. Phys.: Condens. Matter*, 2009, **21**, 395502.

42 J. P. Perdew and K. Burke, *Phys. Rev. B: Condens. Matter Mater. Phys.*, 1996, **54**, 16533–16539.

43 J. K. Nørskov, T. Bligaard, A. Logadottir, J. R. Kitchin, J. G. Chen, S. Pandelov and U. Stimming, *J. Electrochem. Soc.*, 2005, **152**, J23.